Electron-beam-induced ferroelectric domain behavior in the transmission electron microscope: Toward deterministic domain patterning

Hart, J. L., Liu, S., Lang, A. C., Hubert, A., Zukauskas, A., Canalias, C., ... Taheri, M. L. (2016). Electron-beam-induced ferroelectric domain behavior in the transmission electron microscope: Toward deterministic domain patterning. Physical Review B, 94, [174104]. DOI: 10.1103/PhysRevB.94.174104

Published in:
Physical Review B

Document Version:
Peer reviewed version

Electron beam-induced ferroelectric domain behavior in the transmission electron microscope: toward deterministic domain patterning

*James L. Hart[1], Shi Liu[2,3], Andrew C. Lang[1], Alexander Hubert[4], Andrius Zukauskas[5], Carlota Canalias[5], Richard Beanland[4], Andrew M. Rappe[2], Miryam Arredondo[6], Mitra L. Taheri[1]**

1. Department of Materials Science and Engineering, Drexel University, Philadelphia, PA 19104, USA
2. Department of Chemistry, University of Pennsylvania, Philadelphia, PA 19104, USA
3. Geophysical Laboratory, Carnegie Institution for Science, Washington, DC 20015, USA
4. Department of Physics, University of Warwick, Coventry CV4 7AL, UK
5. Department of Applied Physics, KTH - Royal Institute of Technology, 10691 Stockholm, SWE
6. Department of Mathematics and Physics, Queen's University, Belfast BT7 1NN, UK

*corresponding author: mtaheri@coe.drexel.edu

We report on transmission electron microscope beam-induced ferroelectric domain nucleation and motion. While previous observations of this phenomenon have been reported, a consistent theory explaining induced domain response is lacking, and little control over domain behavior has been demonstrated. We identify positive sample charging, a result of Auger and secondary electron emission, as the underlying mechanism driving domain behavior. By converging the electron beam to a focused probe, we demonstrate controlled nucleation of nanoscale domains. Molecular dynamics simulations performed are consistent with experimental results, confirming positive sample charging and reproducing the result of controlled domain nucleation. Furthermore, we discuss the effects of sample geometry and electron irradiation conditions on induced domain response. These findings elucidate past reports of electron beam-induced domain behavior in the transmission electron microscope and provide a path towards more predictive, deterministic domain patterning through electron irradiation.

I. INTRODUCTION

Control over ferroelectric domain structure and switching is necessary for successful implementation of technologically important ferroelectric based devices. For instance, ferroelectric random-access memory requires reliable and high frequency polarization switching, a process ultimately governed by domain kinetics [1]. Other devices, such as periodically poled ferroelectrics for nonlinear optical frequency conversion [2] and ferroelectric photovoltaics using domain walls for current generation [3], rely on specific domain structures for efficient operation. While domain manipulation is conventionally achieved through direct application of an electric field, electron irradiation offers an alternative path for domain control. This effect is well studied and understood for a scanning electron microscope (SEM) electron beam [4–9]; Ferris *et al.* demonstrated nanoscale control over domain structure and explained the results with known sample charging mechanisms [10].

Several reports exist of transmission electron microscope (TEM) electron beam-induced domain behavior, though control over domain response has generally been limited, and several conflicting theories describing induced behavior have been presented [11–16]. Matsumoto and Okamoto observed a 180° in-plane domain pattern transform into a 90° in-plane nanostripe domain structure in a $BaTiO_3$ (BTO) focused ion beam (FIB) sample. Phase field simulations and polarization analysis suggest the presence of an anisotropic in-plane electric field. The authors propose the induced field was generated either from the anisotropic conduction of BTO or anisotropic electrical boundary conditions [11]. Ahluwalia *et al.* observed domain reconfiguration in BTO nanodots and explained the behavior based on negative sample charging; however, the mechanism for negative charging was not identified [12]. In each of these studies, TEM image contrast revealed ferroelastic domains, and the ferroelectric polarization vector associated with each imaged domain could not be fully determined. This ambiguity prevented definitive tracking of beam-induced polarization changes, limiting the understanding of induced electric fields driving domain motion. More recently Chen *et al.* studied $YMnO_3$, a hexagonal ferroelectric with three antiphase domains related to MnO_5 bipyrimidal tilting [16]. Controlled nucleation of ferroelectric domains with a converged electron beam was demonstrated, and the induced domain response was attributed to positive sample charging through secondary electron emission.

To advance the prospect of controlled domain patterning in the TEM, it is vital to understand the nature of induced electric fields driving domain motion, the effects of different electron irradiation conditions, and the role of sample geometry. In this article, these fundamental yet unresolved issues are addressed. We investigate the ferroelectric, non-ferroelastic, Rb-doped $KTiOPO_4$ (RKTP). In contrast to ferroelastic-ferroelectrics such as BTO with six ferroelectric domain variants, RKTP has only two ferroelectric domain variants which we unambiguously identify through a surface etch. Using this simple approach, we show that all induced domain behavior is driven by positive sample charging. We demonstrate that different domain nucleation patterns may be achieved by adjusting electron irradiation conditions, and that proximity to conductive grounds effectively eliminates charging and prevents beam-induced domain behavior. Supporting the results of Chen *et al.*, domains are locally nucleated with high spatial accuracy through use of a converged electron beam. These results represent a step towards greater domain control *via* TEM irradiation with implications for nanoscale device fabrication.

II. MATERIALS AND METHODS

RKTP is a nonlinear optical material used for periodic poling. It possesses an orthorhombic crystal structure [17,18], has a coercive field of 3.7 kV mm^{-1} [19], and has a Curie temperature of 1209 K [20]. RKTP is isomorphic to $KTiOPO_4$ (KTP) and shows similar domain morphology, but the domain dynamics of RKTP differ from KTP due to its reduced ionic conductivity [21] which grants faster domain propagation along its polar axes and reduced domain broadening during periodic poling [22–25]. For this study, a commercial single-crystal flux-grown RKTP sample was periodically poled with an average periodicity of 650 nm using a self-assembling technique [26].

TEM is a technique well suited for *in situ* study of ferroelectric domains [27–31]. For this study, a JEOL LaB_6 2100 TEM was operated at 200 keV with a beam current of ≈1 nA [32]. Domains were observed with dark-field TEM imaging; the sample was tilted to a two-beam condition, and images were acquired from (001) type reflections. TEM samples were prepared *via* a conventional *in situ* liftout process in a dual-beam FIB (FEI DB235) and either placed on a lacy carbon film or attached to a supporting Cu post. Samples were constructed with lateral dimensions of approximately 5×20 μm and thicknesses of 200-300 nm. The [100] axis of RKTP was aligned on the 20 μm edge of the sample, and the [001] axis (the polar axis) was aligned along the 5 μm edge.

Initial domain morphology consisted of c^- domains [polarization pointing down in Fig. 1(a)] in a c^+ matrix [polarization pointing up in Fig. 1(a)], with domain walls on (100) planes. Prior to TEM sample preparation, the bulk RKTP crystal was exposed to a molten salt etch which preferentially attacks the c^- face (c^- domains correspond to domains switched during periodic poling) [33,34]. Owing to the surface etch, each c^- domain is associated with a surface dimple. As shown in Fig. 1(a), this dimple is observed in the TEM along the top edge of the sample next to the protective metal layers (deposited in the FIB before cutting and lifting out the lamella), allowing determination of domain polarity.

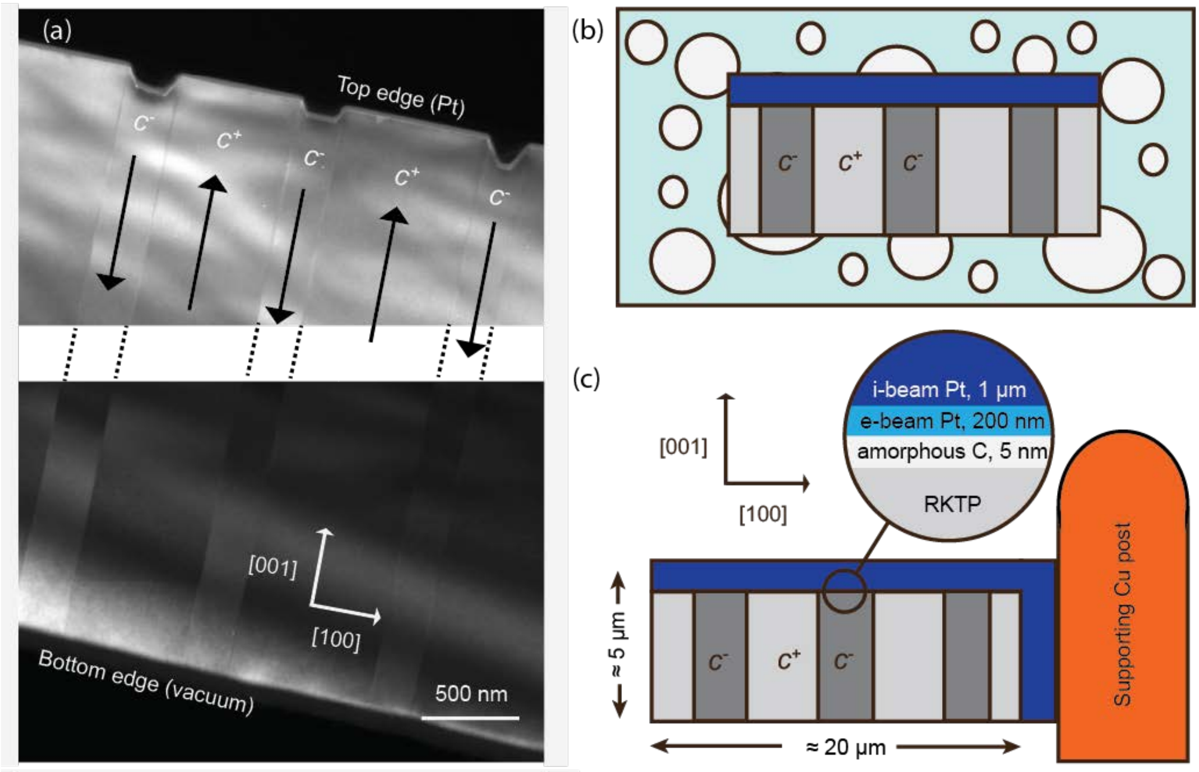

FIG. 1. (a) Dark-field TEM image showing initial domain configuration. Dark arrows represent the ferroelectric polarization. (b) Schematic of RKTP lamella on lacy carbon film, here termed electrically grounded samples. (c) Schematic of RKTP lamella attached to a supporting Cu post, here termed electrically isolated samples. In the TEM image and both schematics, the electron beam is normal to the image.

III. RESULTS AND DISCUSSIONS

A. Transmission Electron Microscope Observations

The role of electrical boundary conditions was investigated by comparing the behavior of electrically-grounded lamellae on lacy carbon support films with that of electrically-isolated lamellae attached to supporting Cu posts. For the samples on lacy carbon, more than 50% of the 5×20 μm face was in contact with the conductive carbon support [Fig. 1(b)]. Samples were exposed to the electron beam for over an hour, and no induced domain response was observed. The carbon film alleviates local sample charging, restricting the build-up of electric fields and preventing induced domain behavior. By contrast, all electrically isolated samples displayed beam-induced domain nucleation and growth. These samples were only grounded along their top and right edges. The right edge was grounded by FIB-deposited Pt, a poor conductor [35]. The top edge was coated with a thin layer of carbon followed by SEM-deposited Pt and lastly FIB-deposited Pt [Fig. 1(c)]. With this geometry, sample charging cannot easily be alleviated, allowing the build-up of charge and induced electric fields.

The electrically isolated samples all exhibited similar behavior. Under uniform irradiation, a condition achieved by spreading the electron beam to evenly irradiate the entire sample, c^- domain area decreased along the top edge of the sample and simultaneously increased along the bottom edge. The left panels of Fig. 2(a) shows the intersection of a single c^- domain with the top and bottom sample edges, and the right panels shows the same domain after 1 hour of uniform irradiation. The c^- domain retracts from the top edge and increases in area along the bottom edge. The intermediate domain structure along the sample bottom edge between t = 0 and t = 1 hour was not observed for this particular domain; however, instances of lateral expansion of individual c^- domains has been observed, as has the nucleation, propagation, and merger of multiple c^- domains. Nucleation of multiple c^- domains along the bottom edge is shown in Fig. 2(b) and appear similar to KTP domain switching observed with digital holography [23]. The extent that c^- domains retracted from the top edge varied between domains; Fig. 2(c) shows a domain which retracted over 1 μm after 1 hour of irradiation. Digital large-angle convergent beam electron diffraction (D-LACBED) [36] was used to definitively confirm that the contrast observed in dark-field TEM was due to an altered ferroelectric domain structure [37]. While not every c^- domain withdrew from the top edge or expanded along the bottom edge when subjected to uniform irradiation, there were no instances of c^- domain growth along the top edge or c^- retraction from the bottom edge.

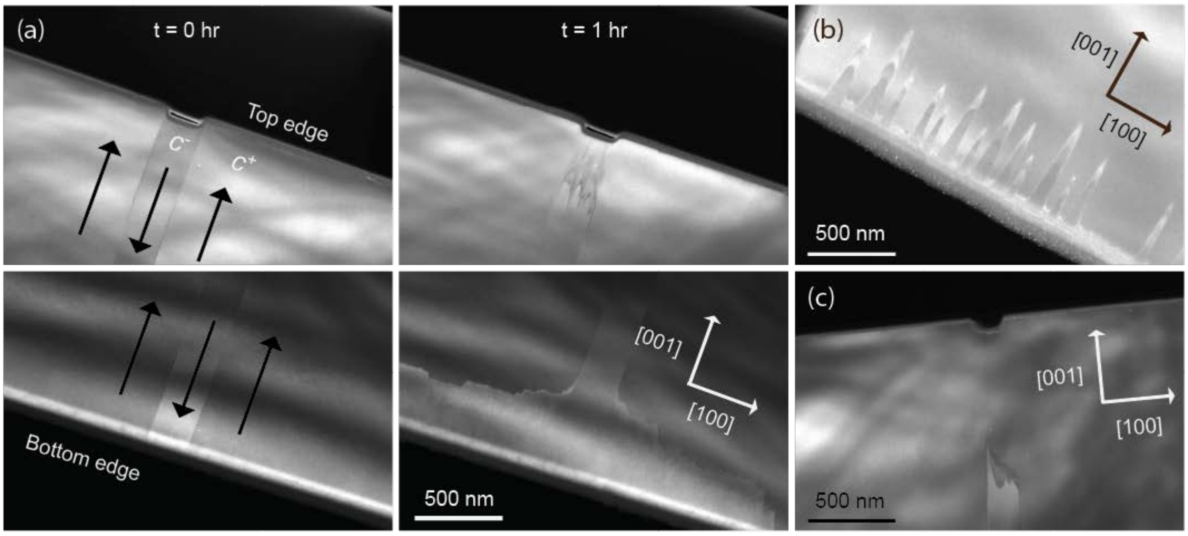

FIG. 2. (a) Dark-field TEM images showing electron beam-induced domain motion after 1 hour of uniform irradiation. The dark arrows indicate domain polarization. All panels show the same domain. Top panel images show where the domain intersects the top edge, and the bottom panel images show where the domain intersects the bottom edge. (b) Observation of multiple c^- domain nucleation sites along the bottom edge after uniform irradiation. (c) A c^- domain which retracted 1 μm from the top edge after 1 hour of uniform irradiation.

Under non-uniform irradiation, where the electron beam was focused to selectively irradiate a small area, the induced domain behavior was entirely different. Non-uniform irradiation produced nucleation within the sample interior, local to the area of irradiation. When the electron beam was converged to a diameter of 2 μm and placed within a c^+ domain for 5 minutes, multiple c^- domains nucleated along the bottom of the electron beam perimeter [Fig. 3(a)]. When the electron beam was further converged within a c^+ domain, individual c^- domains were nucleated. Figures 3(b) and 3(c) show two instances of domain nucleation from converged electron beams of 400 and 100 nm diameter, respectively. Although non-uniform irradiation did not always produce c^- domain nucleation, no cases of nucleation along the sides or top of the irradiated area were observed. Due to relatively large specimen thicknesses in these areas (>300 nm), D-LACBED was not able to confirm that the observed contrast in dark-field imaging corresponded to nucleated c^- domains. In place of D-LACBED, a nanobeam-diffraction pattern was acquired from within the presumed c^- domain shown in Fig. 3(b); the pattern is shown in the inset. The pattern shows crystalline order and matches diffraction patterns acquired from the adjacent c^+ matrix. This result rules out the possibility of amorphization or recrystallization producing the observed contrast. Since beam-induced electric fields and heating should be radially symmetric [38], the asymmetric sample response suggests a sample asymmetry is responsible for the contrast. The obvious asymmetry is sample polarity, indicating the observed contrast corresponds to nucleated c^- domains.

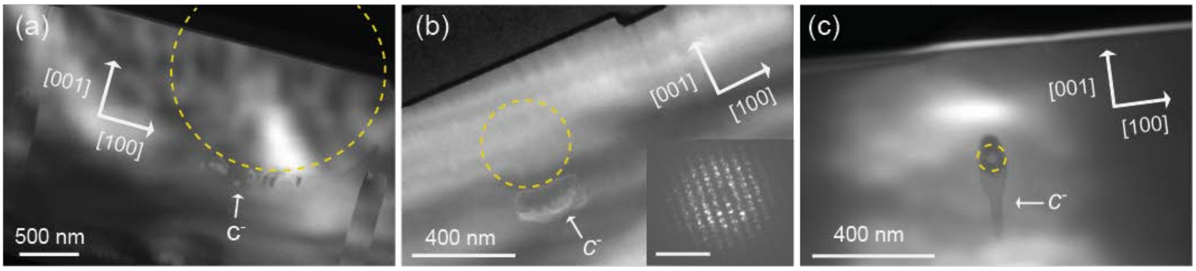

FIG. 3. Dark-field TEM images show c^- domain nucleation within a c^+ domain after 5 minutes of non-uniform irradiation applied with a converged electron beam. The dotted circles represent placement and approximate size of the electron beam. (a) Multiple domains nucleated from a converged beam of 2 μm diameter. (b) Domain nucleated from a converged beam of 400 nm diameter with a nanobeam-diffraction pattern of the induced c^- domain shown in the inset. The scale bar in the inset is 5 nm^{-1}. (c) Domain nucleated from a converged beam of 100 nm diameter. A ring of carbon deposited by the electron beam is observed along the beam perimeter.

As noted above, the degree of induced domain motion varied from sample to sample. Several factors may have contributed to this variation. FIB sample preparation creates surfaces with a thin amorphous layer of Ga implantation [39]. Defects in ferroelectrics can act both to pin ferroelectric domains and lower domain nucleation energy. Thus FIB damage is likely to affect the induced domain motion, and differences in FIB damage could account for the varied behavior between samples. Sample thickness may also play a role. Due to the FIB lift-out procedure, the sample is expected to be thinner along the top edge and thicker along the bottom. Uniform irradiation generally produced domain motion along the top edge before the bottom, possibly due to the thickness gradient resulting from FIB preparation. Such a thickness dependency may also explain the variation in domain switching for different samples (inevitably with slightly different thicknesses) that were irradiated for similar times. Additionally, differences in Rb content could affect domain response. RKTP is an ionic conductor and conductivity is strongly affected by Rb content [18]. It is possible that local variations in Rb doping affected conductivity and thus sample charging, locally altering the induced electric field and domain response [38].

B. Positive Charging Analysis

All observed domain behavior can be explained by positive sample charging (Fig. 4). In the following, the effects of FIB-induced sample damage, nonuniform intensity of the electron beam, thickness variation, non-stoichiometry, and electric contacts along the top and right edges are assumed to be minimal. Beginning with the assumption of positive sample charging induced by the electron beam, uniform irradiation would cause samples to develop a positive charge density. For a conducting sample, the generated positive charge would repel itself towards the sample edges, in turn eliminating internal electric fields. For an insulating ferroelectric sample, positive charge generated within the sample bulk would be fixed in place, allowing the existence of non-equilibrium internal fields. The resulting radial electric field would be strongest along the sample perimeter [40]. Switching would be favored wherever the induced field has a large component antiparallel to the local polarization vector.

For our experimental geometry, the induced field will favor c^+ domain growth along the top edge and c^- domain growth along the bottom edge, as observed experimentally. Near sample edges this radial field will appear anisotropic, potentially explaining the results of Matsumoto and Okamoto who also observed TEM-induced domain motion in FIB prepared lamella [11]. Moreover, if one considers the ambiguity of ferroelastic domain imaging, positive charging and an induced divergent radial field can explain the nanodot domain reconfiguration observed by Ahluwalia *et al* [12]. For non-uniform irradiation, sample charging will only occur under areas of irradiation, producing an electric field directed radially away from the beam and strongest along the perimeter of the irradiated area [40]. This induced field will favor c^+ domain growth above the beam and c^- growth below. If the beam impinges on a c^+ monodomain region, the only induced domain response will be c^- nucleation below the irradiated area, agreeing with the experimental observations shown in Fig. 3.

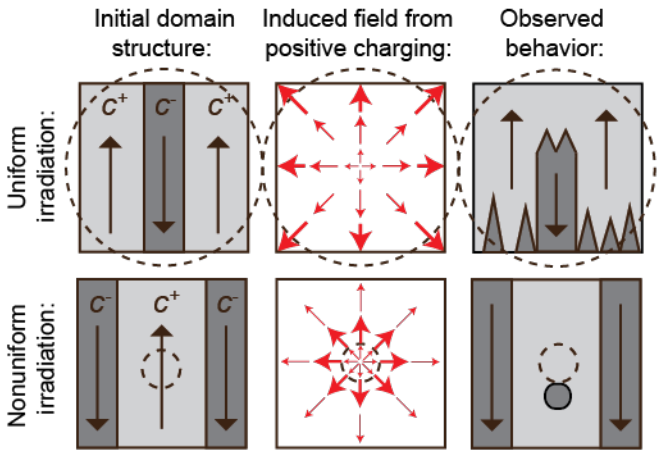

FIG. 4. Schematic showing electric fields due to positive sample charging, alongside observed domain behavior. The dashed circles represent the area of electron irradiation. The arrows in the left and right panels represent ferroelectric polarization, and the arrows in the middle panel represent the induced electric field.

Positive charging is expected for insulating TEM specimens. Despite the irradiation of samples with negative charge carriers, electron absorption is negligible due to the high beam energy and reduced specimen thickness necessary for TEM [38,41,42]. Conversely, positive charge can develop in the form of hole accumulation under areas of irradiation, resulting from Auger and secondary electron emission following inelastic electron scattering [38,41]. Electric fields resulting from positive sample charging have been measured experimentally through contrast transfer function analysis [43,44] and have been observed to cause ion migration and nanoparticle motion [45,46].

As positive charge accumulates under areas of irradiation the local potential will increase. Emission of low energy secondary electrons will diminish, but emission of high kinetic energy Auger electrons will persist. Compensating electric currents within the sample will develop to screen the positive charge. While the rate of Auger emission is proportional to the beam current and is thus constant, the compensating currents will increase as more positive charge accumulates and the induced electric field increases. Eventually a steady-state condition is reached when the compensating electric currents balance the rate of Auger emission. At steady-state, the induced radial electric field along the electron beam perimeter may be calculated with [38]

$$E = \left({I_0}/{2\pi\gamma r} \right) \sum_{i,j} N_i \sigma_{ij} \alpha_{ij} \qquad (1)$$

where I_0 is the incident current, γ is the material conductivity, *r* is the electron beam radius, N_i is the spatial density of atomic species *i*, σ_{ij} is the partial cross-section for atomic species *i* and transition *j*, and α_{ij} is the probability for auger emission for species *i* and transition *j* given the existance of a core hole. The incident current I_0 was 1 nA. The conductivity γ was taken from Ref. [18], and *r* was taken to be 1 μm. The partial cross-sections σ_{ij} were calculated using the Bethe equation as implemented in Egerton's SIGMAK and SIGMAL programs [47]. The probabilities for auger emission α_{ij} were approximated as 0.5 for all edges less than 5 keV, and edges over 5 keV were not considered in the calculation. This approximation is necessarily an underestimation [38], providing a lower bound for the actual Auger yeild. With these values, we calculate an induced electric field of 60 kV mm^{-1}, well above the 3.7 kV mm^{-1} coercive field of RKTP [19].

C. Molecular Dynamic Simulations

Molecular dynamics (MD) simulations were performed which qualitatively reproduce experimental results for both uniform and non-uniform irradiation and support the assignment of positive sample charging. MD simulations can provide detailed dynamic information concerning complex nanoscale events [48–50]. However, for a given material, a predefined force field that describes the interatomic interactions is required to carry out all-atom large-scale MD simulations. As no force field has been developed for RKTP, we study a comparable ferroelectric, $PbTiO_3$ (PTO).

PTO is a classic ferroelectric, with a bond-valence force field parameterized from *ab initio* calculations [51–53]. The supercell for modeling the ferroelectric consisted of an 80-unit-cell-thick (≈165 Å) PTO slab and ≈85 Å of vacuum along the simulation cell *c* axis (out-of-plane). The top of the slab is terminated by a TiO_2 layer and the bottom by a PbO layer [Fig. 5(a)]. TiO_2 and PbO layers have bond-valence charges of -0.58785 and 0.58785 elementary charges per formula unit (e/fu). To stabilize a thin film ferroelectric in vacuum, the charges of the top TiO_2 and bottom PbO layers were reduced by a factor of two. Under this condition, in-plane polarization (*a* domain) is favored over out-of-plane polarization (*c* domain) to minimize the depolarization field. To achieve a non-ferroelastic, c^+ monodomain structure, 0.2 e/fu is added to the top TiO_2 surface layer and 0.2 e/fu is removed from the bottom PbO surface layer. To insert a c^- domain within the c^+ matrix, the process is reversed; 0.2 e/fu is removed from the top TiO_2 surface layer and 0.2 e/fu is added to the bottom PbO surface layer. The resulting structure is shown in Fig 5(a). By stabilizing this initial domain structure and fixing the in-plane lattice constant, the formation of a new domain with polarization along the in-plane *a* axis *via* ferroelastic 90° switching has a significant elastic energy cost; 180° ferroelectric switching is in general favored. In this regard, the PTO simulations with a slab model resemble the ferroelectric, non-ferrolastic, nature of RKTP, allowing qualitative comparison.

The electron irradiation is modeled by changing the charge of atoms to simulate the induced electric fields shown in Fig. 4. The instantaneous local polarization, $\mathrm{P_u}(t)$, for each unit cell (uc) is calculated with

$$P_u(t) = \frac{1}{V_u}\left(\frac{1}{8}Z^*_{Pb}\sum_{i=1}^{8} r_{Pb,i}(t) + Z^*_{Ti} r_{Ti}(t) + \frac{1}{2}Z^*_{O}\sum_{i=1}^{6} r_{O,i}(t)\right) \tag{2}$$

where V_u is the volume of a unit cell, Z^*_{Pb}, Z^*_{Ti}, and Z^*_{O} are the Born effective charges of Pb, Ti, and O atoms, $r_{Pb,i}(t)$, $r_{Ti,i}(t)$, and $r_{O,i}(t)$ are instantaneous atomic positions for Pb, Ti, and O atoms in a unit cell.

To test the effects of uniform sample irradiation of a finite sample, upward [Fig. 5(b)] and downward [Fig. 5(c)] local electric fields were imposed by changing the charge of surface atoms. The solid lines in Fig. 5(b) and 5(c) indicate the specific regions where the surface charges were altered; in both cases the charge was reduced by 0.3 e/fu to generate local fields consistent with positive sample changing illustrated in Fig. 4. The simulated domain responses closely resemble experimental results, showing the retreat of the c^- domain from the top edge and the nucleation of a c^- domain along the bottom. To simulate non-uniform irradiation, a positive charge density of 0.3 e/uc was injected within a monodomain c^+ area, shown in Fig. 5(d). In agreement with experiments, a c^- domain nucleated directly below the area of charge injection, and no switching was observed above or along the edges of the area of charge injection. By comparison, the simulation with a *negative* injected charge density shows a c^- domain nucleating above the region of irradiation [Fig. 5(e)]. This simulation with negative sample charging gives results in complete opposition to experiment, providing further validation that the induced domain behavior is driven by positive, not negative, sample charging.

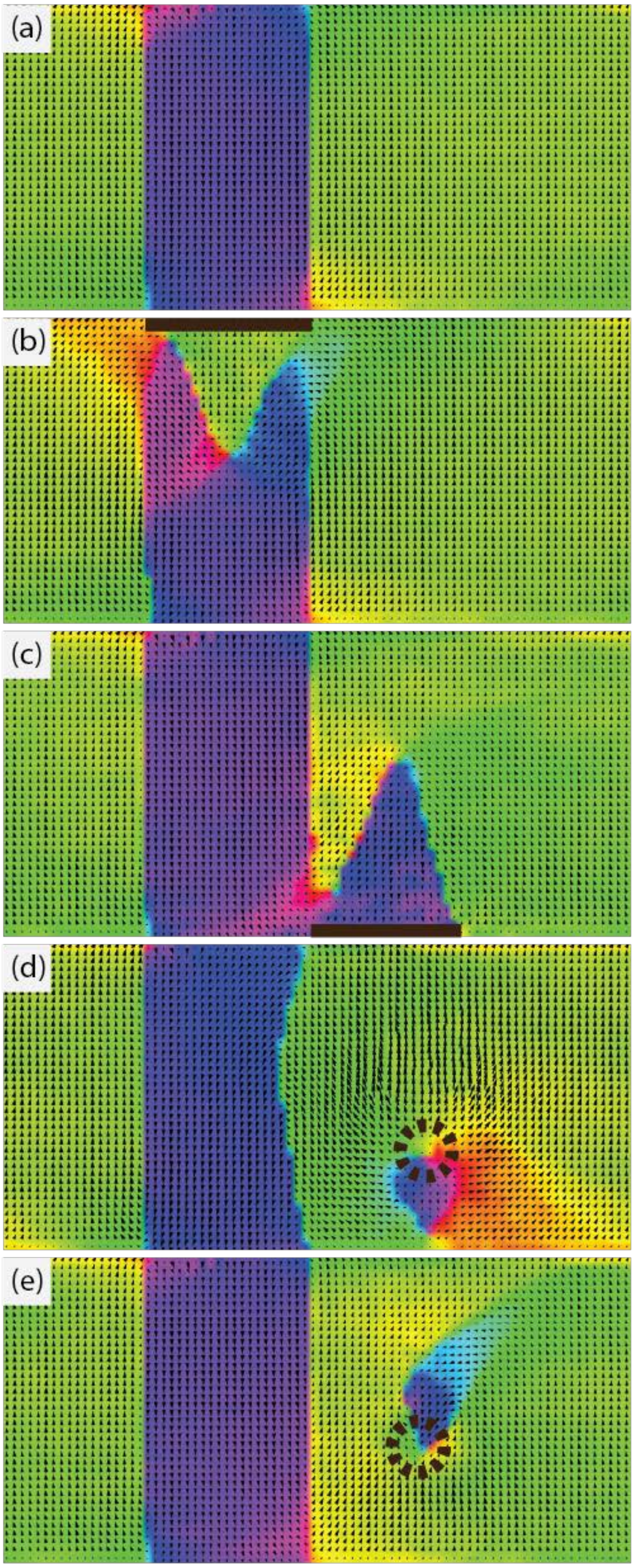

FIG. 5. Molecular dynamics simulations of $PbTiO_3$. (a) Initial domain morphology. (b and c) Simulated domain response to uniform irradiation. The solid black lines indicate where the surface charge was reduced by 0.3 e/fu. (d and e) Simulated domain response to non-uniform

irradiation. In (d) the dashed circle represents a positive charge density of 0.3 e/uc and in (e) the dashed circle represents a negative charge density of 0.3 e/uc. Simulated behavior qualitatively agrees with experimental results.

IV. OUTLOOK AND CONCLUSIONS

With a clear understanding of specimen charging and its relation to induced ferroelectric behavior, the prospect of domain patterning in the TEM is considered. As shown in Fig. 3, localized nucleation of domains with dimensions approaching 100 nm is possible. This domain size is comparable to the lower limit of domain nucleation achieved with an SEM beam [10,54]; however, it is likely that domain patterning in the TEM could be much more precise. In contrast to the SEM, the beam-specimen interaction volume for a focused TEM beam and a thin specimen is on the order of nanometers, suggesting greater control and confinement of the induced electric fields may be achieved. While the TEM electron beam offers an avenue for ultrafine domain manipulation, its use introduces several challenges. Sample irradiation with high energy electrons can lead to sputtering and mass loss through high-angle electron scattering and severe sample charging [55]. Furthermore, the interaction of primary electrons with hydrocarbons present on the sample surface can lead to carbon deposition. These issues may place a limit on the practical longevity of controlled ferroelectric switching in the TEM. Secondly, TEM requires electron transparency thus restricted sample geometries. TEM sample preparation *via* FIB also presents a problem, with Ga implantation and the formation of a thin amorphous surface layer. Such defects will affect ferroelectric properties, though modern FIBs can greatly reduce induced damage by going to lower ion-beam voltages.

In conclusion, we studied TEM electron beam-induced domain nucleation and growth in the ferroelectric RKTP. By linking sample charging mechanisms, induced electric fields, and observed domain responses, we provide a consistent framework for understanding TEM electron beam-induced ferroelectric domain behavior. The roles of electron irradiation conditions and sample geometry were investigated and shown to strongly affect the induced domain response. Furthermore, nanoscale domains were nucleated with high spatial accuracy. This domain control underscores the potential capabilities of TEM for nanoscale ferroelectric domain patterning.

ACKNOWLEDGMENTS

J.L.H., A.C.L., and M.L.T. acknowledge support from the Office of Naval Research under contract number N00014-14-1-0058. S.L. acknowledges the support of the Office of Naval Research under grant N00014-14-1-0761 and the Carnegie Institution for Science. A.M.R. acknowledges the support of the Office of Naval Research under grant N00014-12-1-1033. The authors thank the HPCMO of the DoD for computational support. M.A. acknowledges financial support from the Engineering and Physical Sciences Research Council in the overseas travel grant scheme (EP/M004945/1). C.C. acknowledges financial support from the Swedish Foundation for Strategic Research under grant FFL090016.

REFERENCES

[1] H. Ishiwara, J. Nanosci. Nanotechnol. **12**, 7619 (2012).

[2] V. Pasiskevicius, G. Strömqvist, F. Laurell, and C. Canalias, Opt. Mater. (Amst). **34**, 513 (2012).

[3] J. Seidel, D. Fu, S.-Y. Yang, E. Alarcón-Lladó, J. Wu, R. Ramesh, and J. W. Ager, Phys. Rev. Lett. **107**, 126805 (2011).

[4] R. W. Keys, A. Loni, R. M. De La Rue, C. N. Ironside, and J. H. Marsh, Electron. Lett. **26**, 188 (1990).

[5] A. C. G. Nutt, V. Gopalan, and M. C. Gupta, Appl. Phys. Lett. **60**, 2828 (1992).

[6] M. C. Gupta, W. P. Risk, A. C. G. Nutt, and S. D. Lau, Appl. Phys. Lett. **63**, 1167 (1993).

[7] D. Li and D. A. Bonnell, Annu. Rev. Mater. Res. **38**, 351 (2008).

[8] J. E. Rault, T. O. Menteş, A. Locatelli, and N. Barrett, Sci. Rep. **4**, 6792 (2014).

[9] D. B. Li, D. R. Strachan, J. H. Ferris, and B. A. Bonnell, J. Mater. Res. **21**, 935 (2006).

[10] J. H. Ferris, D. B. Li, S. V. Kalinin, and D. A. Bonnell, Appl. Phys. Lett. **84**, 774 (2004).

[11] T. Matsumoto and M. Okamoto, J. Appl. Phys. **109**, 014104 (2011).

[12] R. Ahluwalia, N. Ng, a. Schilling, R. G. P. McQuaid, D. M. Evans, J. M. Gregg, D. J. Srolovitz, and J. F. Scott, Phys. Rev. Lett. **111**, 165702 (2013).

[13] J. F. Scott and A. Kumar, Appl. Phys. Lett. **105**, 052902 (2014).

[14] R. Beanland and P. a. Thomas, Phys. Rev. B **89**, 174102 (2014).

[15] N. Ng, R. Ahluwalia, A. Kumar, D. J. Srolovitz, P. Chandra, and J. F. Scott, Appl. Phys. Lett. **107**, 152902 (2015).

[16] Z. Chen, X. Wang, S. P. Ringer, and X. Liao, Phys. Rev. Lett. **117**, 027601 (2016).

[17] F. C. Zumsteg, J. D. Bierlein, and T. E. Gier, J. Appl. Phys. **47**, 4980 (1976).

[18] Q. Jiang, P. A. Thomas, K. B. Hutton, and R. C. C. Ward, J. Appl. Phys. **92**, 2717 (2002).

[19] C. Canalias, J. Hirohashi, V. Pasiskevicius, and F. Laurell, J. Appl. Phys. **97**, 124105 (2005).

[20] J. D. Bierlein and H. Vanherzeele, J. Opt. Soc. Am. B **6**, 622 (1989).

[21] A. Zukauskas, V. Pasiskevicius, and C. Canalias, Opt. Express **21**, 1395 (2013).

[22] C. Canalias, S. Wang, V. Pasiskevicius, and F. Laurell, Appl. Phys. Lett. **88**, 032905 (2006).

[23] C. Canalias, V. Pasiskevicius, F. Laurell, S. Grilli, P. Ferraro, and P. De Natale, J. Appl. Phys. **102**, 064105 (2007).

[24] A. Zukauskas, G. Strömqvist, V. Pasiskevicius, F. Laurell, M. Fokine, and C. Canalias, Opt. Mater. Express **1**, 1319 (2011).

[25] G. Lindgren, A. Zukauskas, V. Pasiskevicius, F. Laurell, and C. Canalias, Opt. Express **23**, 20332 (2015).

[26] A. Zukauskas, V. Pasiskevicius, and C. Canalias, Appl. Phys. Lett. **103**, 252905 (2013).

[27] C. T. Nelson, P. Gao, J. R. Jokisaari, C. Heikes, C. Adamo, A. Melville, S.-H. Baek, C. M. Folkman, B. Winchester, Y. Gu, Y. Liu, K. Zhang, E. Wang, J. Li, L.-Q. Chen, C.-B. Eom, D. G. Schlom, and X. Pan, Science **334**, 968 (2011).

[28] C. R. Winkler, M. L. Jablonski, K. Ashraf, A. R. Damodaran, K. Jambunathan, J. L. Hart, J. G. Wen, D. J. Miller, L. W. Martin, S. Salahuddin, and M. L. Taheri, Nano Lett. **14**, 3617 (2014).

[29] C. R. Winkler, A. R. Damodaran, J. Karthik, L. W. Martin, and M. L. Taheri, Micron **43**, 1121 (2012).

[30] C. Ma and X. Tan, J. Am. Ceram. Soc. **94**, 4040 (2011).

[31] C. R. Winkler, M. L. Jablonski, A. R. Damodaran, K. Jambunathan, L. W. Martin, and M. L. Taheri, J. Appl. Phys. **112**, (2012).

[32] See Supplemental Material at [URL will be inserted by publisher] for procedure used to measure beam current.

[33] F. Laurell, M. G. Roelofs, W. Bindloss, H. Hsiung, A. Suna, and J. D. Bierlein, J. Appl. Phys. **71**, 4664 (1992).

[34] M. C. Gupta, W. P. Risk, A. C. G. Nutt, and S. D. Lau, Appl. Phys. Lett. **63**, 1167 (1993).

[35] Y. J. Ma, Adv. Mater. Res. **652-654**, 339 (2013).

[36] R. Beanland, P. J. Thomas, D. I. Woodward, P. A. Thomas, and R. A. Roemer, Acta Crystallogr. Sect. A Found. Crystallogr. **69**, 427 (2013).

[37] See Supplemental Material at [URL will be inserted by publisher] for D-LACBED analysis concerning domain polarization.

[38] J. Cazaux, Ultramicroscopy **60**, 411 (1995).

[39] L. A. Giannuzzi and F. A. Stevie, Micron **30**, 197 (1999).

[40] D. Griffiths, *Introduction to Electrodynamics*, 3rd ed. (Prentice Hall, Upper Saddle River, NJ, 1999).

[41] R. F. Egerton, P. Li, and M. Malac, Micron **35**, 399 (2004).

[42] D. B. Williams and C. B. Carter, *Transmission Electron Microscopy*, 2nd ed. (Spring Science + Business Media, New York, 2009).

[43] K. Danov, R. Danev, and K. Nagayama, Ultramicroscopy **87**, 45 (2001).

[44] K. Danov, R. Danev, and K. Nagayama, Ultramicroscopy **90**, 85 (2002).

[45] N. Jiang and J. C. H. Spence, J. Nucl. Mater. **403**, 147 (2010).

[46] E. F. White, M. Mecklenburg, B. Shevitski, S. B. Singer, and B. C. Regan, Langmuir **28**, 3695 (2012).

[47] R. F. Egerton, *Electron Energy-Loss Spectroscopy in the Electron Microscope* (Springer US, Boston, MA, 2011).

[48] S. Liu, I. Grinberg, and A. M. Rappe, Appl. Phys. Lett. **103**, 232907 (2013).

[49] R. Xu, S. Liu, I. Grinberg, J. Karthik, A. R. Damodaran, A. M. Rappe, and L. W. Martin, Nat. Mater. **14**, 79 (2015).

[50] Y.-H. Shin, I. Grinberg, I.-W. Chen, and A. M. Rappe, Nature **449**, 881 (2007).

[51] Y.-H. Shin, V. R. Cooper, I. Grinberg, and A. M. Rappe, Phys. Rev. B **71**, 054104 (2005).

[52] S. Liu, I. Grinberg, and A. M. Rappe, J. Phys. Condens. Matter **25**, 102202 (2013).

[53] S. Liu, I. Grinberg, H. Takenaka, and A. M. Rappe, Phys. Rev. B **88**, 104012 (2013).

[54] X. Li, K. Terabe, H. Hatano, and K. Kitamura, Jpn. J. Appl. Phys. **45**, L399 (2006).

[55] R. F. Egerton, P. Li, and M. Malac, Micron **35**, 399 (2004).